

JWST MIRI/MRS in-flight absolute flux calibration and tailored fringe correction for unresolved sources

Danny Gasman¹, Ioannis Argyriou¹, G. C. Sloan^{2,3}, Bernhard Aringer⁴, Javier Álvarez-Márquez⁵, Ori Fox², Alistair Glasse⁶, Adrian Glauser⁷, Olivia C. Jones⁶, Kay Justtanont⁸, Patrick J. Kavanagh⁹, Pamela Klaassen⁶, Alvaro Labiano^{5,10}, Kirsten Larson², David R. Law², Michael Mueller¹¹, Omnarayani Nayak², Alberto Noriega-Crespo², Polychronis Patapis⁷, Pierre Royer¹, and Bart Vandenbussche¹

¹ Institute of Astronomy, KU Leuven, Celestijnenlaan 200D, 3001 Leuven, Belgium

² Space Telescope Science Institute, 3700 San Martin Drive, Baltimore, MD 21218, USA.

³ Department of Physics and Astronomy, Univ. of North Carolina at Chapel Hill, Chapel Hill, NC 27599-3255, USA

⁴ Department of Astrophysics, Univ. of Vienna, Türkenschanzstraße 17, A-1180 Wien, Austria

⁵ Centro de Astrobiología (CAB), CSIC-INTA, ESAC, Carretera de Ajalvir km4, 28850 Torrejón de Ardoz, Madrid, Spain

⁶ UK Astronomy Technology Centre, ROE, Blackford Hill, Edinburgh, EH9 3HJ, UK

⁷ Institute for Particle Physics and Astrophysics, ETH Zurich, Wolfgang-Pauli-Str 27, 8093 Zurich, Switzerland

⁸ Dept. of Space, Earth and Environment, Chalmers University of Technology, Onsala Space Observatory, S-43992 Onsala, Sweden

⁹ School of Cosmic Physics, Dublin Institute for Advanced Studies, 31 Fitzwilliam Place, Dublin 2, Ireland

¹⁰ Telespazio UK for the European Space Agency, ESAC, Camino Bajo del Castillo s/n, 28692 Villanueva de la Cañada, Spain

¹¹ Kapteyn Astronomical Institute, Rijksuniversiteit Groningen, Postbus 800, 9700AV Groningen, Netherlands
e-mail: danny.gasman@ku.leuven.be

Received December 8, 2022

ABSTRACT

Context. The Medium Resolution Spectrometer (MRS) is one of the four observing modes of JWST/MIRI. Using JWST in-flight data of unresolved (point) sources, we can derive the MRS absolute spectral response function (ASRF) starting from raw data. Spectral fringing, caused by coherent reflections inside the detector arrays, plays a critical role in the derivation and interpretation of the MRS ASRF.

Aims. In this paper, we present an alternative way to calibrate the data. Firstly, we derive a fringe correction that accounts for the dependence of the fringe properties on the MIRI pupil illumination and detector pixel sampling of the point spread function. Secondly, we derive the MRS ASRF using an absolute flux calibrator observed across the full 5 to 28 μm wavelength range of the MRS. Thirdly, we apply the new ASRF to the spectrum of a G dwarf and compare with the output of the JWST/MIRI default data reduction pipeline. Finally, we examine the impact of the different fringe corrections on the detectability of molecular features in the G dwarf and K giant.

Methods. The absolute flux calibrator HD 163466 (A-star) is used to derive tailored point source fringe flats at each of the default dither locations of the MRS. The fringe-corrected point source integrated spectrum of HD 163466 is used to derive the MRS ASRF using a theoretical model for the stellar continuum. A cross-correlation is run to quantify the uncertainty on the detection of CO, SiO, and OH in the K giant and CO in the G dwarf for different fringe corrections.

Results. The point-source-tailored fringe correction and ASRF are found to perform at the same level as the current corrections, beating down the fringe contrast to the sub-percent level in the G dwarf in the longer wavelengths, whilst mitigating the alteration of real molecular features. The same tailored solutions can be applied to other MRS unresolved targets. Target acquisition is required to ensure the pointing is accurate enough to apply this method. A pointing repeatability issue in the MRS limits the effectiveness of the tailored fringe flats at short wavelengths. Finally, resulting spectra require no scaling to make the sub-bands match, and a dichroic spectral leak at 12.2 micron is removed.

Key words. Astronomical instrumentation, methods and techniques – Instrumentation: spectrographs – Instrumentation: detectors – Methods: data analysis – Infrared: stars

1. Introduction

During the six-month commissioning phase after the launch of the James Webb Space Telescope (JWST, Gardner et al. 2006; Rigby et al. 2022), the Medium Resolution integral field Spectrometer (MRS, Wells et al. 2015) of the Mid-Infrared Instrument (MIRI, Wright et al., submitted) observed a variety of targets for the purpose of verifying its scientific performance (Argyriou et al., in prep.). The commissioning targets included spatially unresolved (point) sources, namely stars with different ef-

fective temperatures, as well as spatially resolved sources, such as galaxies and planetary nebulae; and it has since been the topic of a variety of scientific work (e.g. Yang et al. 2022; García-Bernete et al. 2022; Miles et al. 2022; Álvarez-Márquez et al. 2022; Lau et al. 2022).

The MRS is an integral field spectrometer, meaning it provides both spatial and spectral information. The 5–28 μm range of the MRS is divided in four channels (labelled 1–4 with increasing wavelength), each divided into three sub-bands (labelled A–C with increasing wavelength). After reducing the data

separately per sub-band, this results in twelve separate spectral "cubes", with two spatial axes, and one spectral (see Law et al., in prep.).

In the spectral direction, MIRI MRS shows high amplitude fringes caused by Fabry-Pérot interference between the reflective layers of the detectors, the depth of which can cause errors up to 30% of the total flux (Argyriou et al. 2020a,b). Fringing has been a systemic issue for instruments on other space telescopes, such as the Space Telescope Imaging Spectrograph on board the *Hubble Space Telescope* (Malumuth et al. 2003), the Short Wavelength Spectrometer on board the *Infrared Space Observatory* (Kester et al. 2003), and the InfraRed Spectrograph (IRS) on board *Spitzer* (Lahuis & van Dishoeck 2000; Lahuis & Boogert 2003). The MRS spectral resolution of 4000-1500 over the 5 to 28 μm wavelength range (Labiano et al. 2021), together with the $\sim 500 \mu\text{m}$ -thick detectors result in the fringe frequencies being spectrally resolved.

The current *JWST* data reduction pipeline (v1.8.3)¹ contains two methods to remove fringes from MRS spectra (a first description of the pipeline can be found in Labiano et al. 2016): a fringe flat derived from spatially extended sources (Mueller et al., in prep), and a residual fringe correction that iteratively finds and removes remaining periodic features in the spectrum that match the expected fringe frequencies based on the geometric and refractive properties of the detectors (Kavanagh et al., in prep).

When observing unresolved sources, the MIRI pupil is non-uniformly illuminated. This causes a significant change in the fringe depth and phase as a function of the part of the point spread function (PSF) that is sampled by the detector pixels (Argyriou et al. 2020b). For spatially extended sources, the MIRI pupil is uniformly illuminated and the fringe properties average out, varying primarily with wavelength. The effectiveness of applying a 2D static fringe flat, derived from a spatially extended source (uniform pupil illumination), to correct the fringes of an unresolved point source (non-uniform pupil illumination) is limited by the underlying physics in question, and can substantially change the pristine shape of the fringes. Applying a residual fringe correction removes periodicities in the range of the detector-induced frequencies, but due to the empirical nature of the correction, it cannot recover the intrinsic detector absolute spectral response function (ASRF).

A challenging science case where a precise fringe correction is required is when looking at sources with dense molecular bands in the mid-infrared. The molecular bands may be identified as fringes by the residual fringe correction algorithm, resulting in removal of real features in the process, or cause the algorithm to fail to identify and remove fringes. As such, we seek to derive a tailored point source fringe flat, henceforth PSFF (acronym chosen to impress the link between the instrumental PSF and the fringes), from a spectrally "boring" source: a predominantly featureless flux calibration standard placed in the exact same position on the detector as a science target of interest. Consequently, however, a tailored ASRF must also be derived based on the defined PSFF, both being intrinsically connected.

The relative spectral response function (RSRF) of the MRS detectors was initially derived on the ground during the MIRI flight model (FM) test campaign. Due to various problems with the test set-up (for more details see Argyriou (2021), and Sect. 2.5 in this paper), systematics were introduced into the spectrophotometric calibration files. During commissioning, the MRS ASRF was derived by applying a 1D correction to the 2D

spectrophotometric response on the detector image plane derived during the FM test campaign. The 1D correction was derived by extracting the point source integrated spectrum of HD 163466 using the ground RSRF, estimating the spectral continuum, and dividing the spectral flux density of the estimated continuum by the values expected based on a theoretical model of the continuum of HD 163466 (Bohlin et al. 2017, 2020). As a result, some of the systematic uncertainties linked to the ground RSRF are still present in the MRS reference files used to calibrate MRS in flight data.

To address the two issues mentioned above, this paper aims to do two things. Firstly, we present the derivation of the PSFF; a fringe flat tailored to unresolved sources. Secondly, we present the derivation of a tailored ASRF solution built from spectrophotometrically uncalibrated data.

With the new PSFF and ASRF solutions at hand, we will use the MRS spectra of HD 37122 and HD 159222 as our two test cases. The K giant star HD 37122 was observed during commissioning as part of the target acquisition test; and the solar analogue G dwarf HD 159222 was one of the targets used to examine the MRS spectrophotometric sensitivity and stability, alongside the previously mentioned A-star HD 163466 (Gordon et al. 2022).

The effect of the fringe corrections implemented in the *JWST* data reduction pipeline, and the PSFF, are compared on in-flight MRS data. To quantify how well the different methods perform, and discuss the implications on the science, we perform cross-correlations to compare the K giant spectra to the synthetic molecular spectra of CO, SiO, and OH, all of which are expected to be detectable (Decin et al. 2003; Sloan et al. 2015); and CO with the G dwarf, which should be present in a star of this spectral type (Heras et al. 2002; Ardila et al. 2010).

In Sect. 2 we describe the MRS in flight observations used in this paper, how the PSFF files are derived, and the different methods of reducing the in flight data. In addition, we describe and illustrate how the MRS ASRF solution is derived, including the correction of a spectral leak feature at 12.2 μm . In Sect. 3 we show the fringe-and-ASRF calibrated spectra. Their implications on the cross-correlation results as well as the science of sources rich in molecular bands is discussed in Sect. 4. Finally, we present our conclusions in Sect. 5.

2. Methods

2.1. Data used

Table 1 gives the information for each of the observing programs carried out during commissioning for the targets used in this paper. This includes the Program Identification numbers (PIDs) from the Astronomer Proposal Tool (APT)².

HD 37122 is a K2III C star located in the Large Magellanic Cloud (LMC) and observed as part of the Surveying the Agents of a Galaxy's Evolution (SAGE) survey (Meixner et al. 2006). K stars have been used as spectrophotometric calibrators in the past, for example for *Spitzer* (Houck et al. 2004), by comparing to spectral templates (Cohen et al. 2003) and synthetic spectra (Decin et al. 2004). However, Sloan et al. (2015) suggest that our current inability to predict the strength of molecular bands in K giants makes them less suited for calibration purposes due to the wealth of molecular bands including CO, SiO, and OH. Instead, HD 37122 was used to test the target acquisition of MIRI MRS,

² <https://www.stsci.edu/scientific-community/software/astronomers-proposal-tool-apt>

¹ <https://jwst-pipeline.readthedocs.io/en/latest/>

Table 1. Properties and programme information of the two stars examined in this work. 1: Gaia Collaboration et al. (2016, 2021); Fabricius et al. (2021); 2: Gray et al. (2003).

ID	HD 37122 ¹	HD 159222 ²	HD 163466 ²
RA	05 30 00.7691	17 32 00.9923	17 52 25.3741
DEC	-69 58 31.871	+34 16 16.131	+60 23 46.94
Spectral type	K2III C	G1V	A7Vm
T_{eff} [K]	~4000	5790	~9000
K mag	5.13	5.05	6.34
APT PID	1029	1050	1050
PI	A. Glasse	B. Vandenbussche	"
Date	May 22-23, 2022	(first visit) June 13, 2022 (repeat visit)	June 8-9, 2022
Dithers ³	4 (positive) 4 (negative)	4 (negative)	4 (positive) 4 (negative)
Groups/integrations (per sub-band)	12/7 (1/2 A, B) 15/6 (1/2 C) 30/3 (3/4) 249.754	15/6 (1/2) 45/2 (3/4)	50/2
Time per dither [s]	263.629 255.304	263.629 252.529	1121.116
Dithers		1050 background 2 (negative)	
Groups/integrations		50/2	
Time per dither [s]		560.558	

due to its brightness in the mid-infrared. HD 159222 has been thought to be a representative Solar analogue, in terms of age and spectrophotometric properties (Soubiran & Triaud 2004; Mahdi et al. 2016), however, Porto de Mello et al. (2014) find that it has a higher temperature, higher metal abundances, and is overall more evolved than the Sun.

2.2. Fringe flats and residual fringe correction

The fringe flats contain the normalised fringe pattern for each MRS spectral band across the detector image plane. The *JWST* pipeline divides the signal on the detector image plane by the fringe flats. For the MIRI MRS these have been derived by fitting sinusoidal models of the MRS fringe pattern to observations of spatially extended sources. Above 10 μm , the fringe flats were derived based on observations of the Cat’s eye nebula (NGC 6543, APT PID 1047). At shorter wavelengths, where the signal-to-noise ratio (SNR) of the NGC 6543 was insufficient, no update to the fringe flats was derived, hence they are based on the FM ground test campaign solutions. Due to the beating of two frequencies produced in different layers of the MRS detectors (Argyriou et al. 2020b) the fringe flats are least accurate in the 10 to 13 μm region. In addition, a third fringe component occurs in the MRS dichroic filters, evident as a very low amplitude high frequency fringes above 11.5 μm , which the fringe flat does not incorporate.

The fringe flat correction reduces the contrast of the fringes, but residuals will remain as described in Sect. 1. `residual_fringe` correction uses an empirical sine model fitting method (e.g. Kester et al. 2003) to further reduce the contrast of the fringing, under the assumption that the residual fringes are small in amplitude following correction by the fringe flat. To prevent the removal of spectral features in the fitting process, an automated spectral feature finding algorithm is used. The algorithm computes a periodogram from a spectrum and looks for prominent frequencies to remove in a range based on the under-

standing of the geometric and refractive properties of the MRS detectors. A Bayesian evidence loop is then used to identify the optimum number of sinusoids to include in the fit in order to prevent over-fitting (Kavanagh et al., in prep.). This algorithm can be applied directly after the *JWST* pipeline fringe step, in 2D, and/or after spectral extraction, in 1D. For this work we apply both the 2D correction at the end of the `calspec2` module of the pipeline, and the post-pipeline residual fringe correction, i.e. on the 1D extracted spectrum, in order to be consistent with how the vast majority of MIRI science teams are reducing the MRS data. Taken together, the fringe flat and the residual fringe correction are expected to reduce fringe contrast to below 6% across the MRS wavelength range (Argyriou et al., in prep.). A significant portion of MIRI science programmes require an uncertainty on the continuum below 1% (SNR of 300 for a 3- σ detection).

2.3. PSFF: Fringe flat tailored to unresolved (point) sources

The source used for the purpose of deriving the PSFF reference files is the A-star HD 163466. We have already discussed that the fringe pattern of an unresolved source depends on how the incoming wavefront from the MIRI pupil, on the detector, is sampled by the detector pixels. The quality of an empirically derived fringe flat for an unresolved source is limited by our ability to reproduce the sub-pixel pointing between calibrator (e.g. HD 163466) and the science target of interest. The left panel in Fig. 1 shows a part of the fringe flat at the centre of the PSF for different detector columns (offsets in X-pixel direction, PSF centre with offset=0), and demonstrates that both the depth and phase change depending on the part of the PSF that is sampled. In the right panel, the 2-dimensional fringe flat is shown, where this phase shift is clearly visible as two diagonal zebra patterns. In the case where the MIRI pupil is illuminated uniformly (extended source illumination) the zebra stripes are approximately horizontal (Argyriou et al. 2020b).

To produce a PSFF for the unresolved source HD 163466, spectral features were removed from the data using `sigma_clip` in *Astropy* (Astropy Collaboration et al. 2013, 2018) with $\sigma = 3$, after which the continuum was removed per detector column using a running mean. Any clipped sections are set to a value of 1. Due to the way the light is sliced and dispersed onto the detectors by the MRS optics, the signal is curved (it does not follow vertical columns). This results in a rapid change in signal at the top and bottom of the detector and edge effects have to be omitted.

As shown in the right panel of Fig. 1, the part of the detector observing background is flat and noisy in the derived fringe flat. In parallel, the parts of the detector on which the source is dispersed show the zebra pattern corresponding to fringe peaks and troughs. These peaks and troughs, due to dividing by the continuum, are now expressed in fringe depth as a fraction of the assumed continuum. We omit applying noise filtering as this affects the extracted fringe pattern, especially at the edges of the PSF and at longer MRS wavelengths where the SNR is lower.

In this work, the PSFF is only applied to the G dwarf, and not the K giant. The K giant data was taken earlier in commissioning, prior to an update to the instrument’s astrometric calibration. This causes the pointing to be inconsistent with the current pattern, and the offset to be larger than a pixel. Though we cannot yet constrain the necessary pointing accuracy of the MRS due to the limited amount of available in flight data, the pointing repeatability must at least be accurate to within half a pixel. Since the performance of the PSFF correction is limited by the pointing, the large offset between the K giant and the calibrator means

³ <https://jwst-docs.stsci.edu/jwst-mid-infrared-instrument/miri-operations/miri-dithering/miri-mrs-dithering>

that the PSFF cannot be used in this case. However, due to the presence of dense molecular bands, it is a perfect test case for the removal of molecular features by the residual fringe correction.

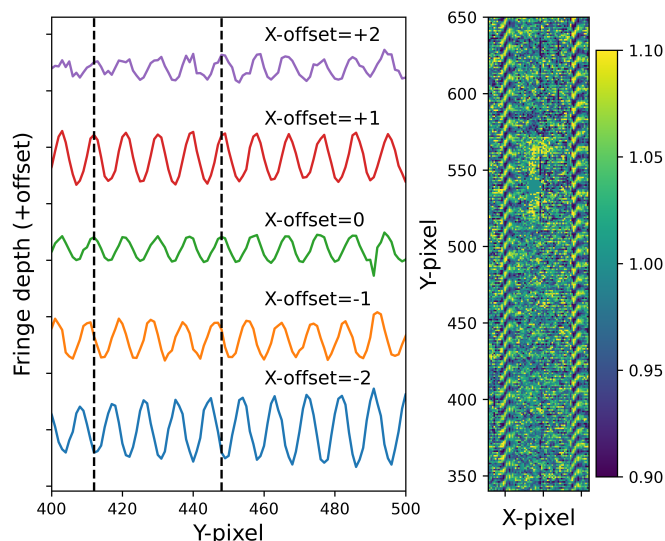


Fig. 1. Change in fringe pattern with X-pixel offset from PSF peak (left), and selected area of the fringe flat detector image (right). The data in the left panel is offset with respect to each other in the y-direction by 0.4, and the black vertical lines are the location of two fringe peaks at X-offset=1. The change in phase is visible in both the left and right panels, while the change in depth is most visible on the left.

2.4. Spectral extraction

The data from each observing programme were reduced using the *JWST* calibration pipeline v1.8.3, where the outlier rejection in step 3 was skipped (this step has been found to give spurious results due to the spatially undersampled PSF). 1D spectra were extracted from the MRS 3D spectral cubes created using a 3D drizzling algorithm (Law et al. in prep.). The default 1D extraction of the *JWST* pipeline was skipped. Instead, we extracted the spectra from the cubes manually, using a growing circular aperture centred on the PSF of 2.5 times λ/D at each wavelength (radii from 0.470–2.757 arcsec). A growing circular annulus was defined to subtract the background. The photometric extraction is illustrated in Fig. 2. To compute the 1D integrated point source spectrum, the signal within the aperture is summed, and the median signal in the annulus, scaled by the aperture area, is subtracted. An aperture correction factor is applied to account for the flux not included in the aperture as well as the fraction of the PSF present inside the annulus. These values are consistent with the ones presented in Argyriou et al., in prep.

2.5. Spectrophotometric calibration and the PSFF

Before we can discuss the performance of the different fringe corrections, first the spectrophotometric calibration solution must be discussed, as this is influenced by the choice of fringe flat applied.

We mentioned that the commissioning spectrophotometric calibration files are plagued by systematics introduced by ground testing. In Argyriou (2021) the systematic uncertainties linked to the ground RSRF solutions are discussed. We provide a sum-

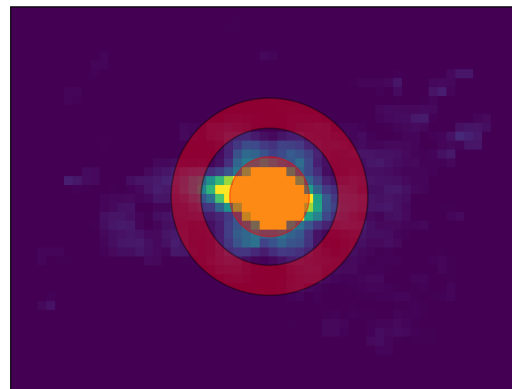


Fig. 2. Example showing a cube image of band 1A image with a circular aperture and annulus overlaid.

mary here, along with the corresponding section in Argyriou (2021) in parenthesis:

- The MRS RSRF was derived using a blackbody source that produced a spatially homogeneous extended illumination pattern on the detectors. Based on these observations, a set of 2D static fringe flats was derived and these flats were used as the reference fringe correction for all subsequent datasets collected over the multiple *JWST*/MIRI test campaigns that followed (Sect. 6.2 and 7.1.3).
- In order to derive the MRS RSRF, assumptions were made about the spectral flux density of the calibration source (blackbody model), the geometry of the illumination by the MIRI Telescope Simulator (MTS) reaching the MIRI pupil, as well as the reflectivity curves of the MTS surfaces (Sect. 7.1.1).
- A water feature was present at $8\ \mu\text{m}$, which was folded into the MRS RSRF (Sect. 7.1.3).
- Electronic ghosts introduced part of the flux measured in detector column c to detector column $c + 4$ (Sect. 2.4.2).

In order to extract a point source spectrum with the correct values of spectral flux density (in units of Jansky), a precise and accurate spectrophotometric response solution (henceforth PHOTOM) is required. Assuming the detector electronic effects are well-calibrated in the *JWST* `calwebb_detector1` module of the pipeline (Morrison et al., in prep.), a subtle yet fundamental aspect of applying a set of PHOTOM files, is that the best results are produced when observing a star with the (a) same number of dithers as the absolute flux standard that was used to derive PHOTOM, (b) the same aperture size and aperture correction, and (c) the same fringe correction. Applying a different fringe correction means that a new set of PHOTOM files need to be derived, as the fringes and PHOTOM are linked. The fringe flats incorporated in the *JWST* pipeline assume that the peaks of the fringes are the true signal; an example is shown in Fig. 3, where a transmission value of 1 is set at the location of the fringe peaks. The uncalibrated data are divided by this fringe flat, bringing the entire spectrum "up" at the fringe peaks, assuming this to be the "true" flux. The PSFF derived Sect. 2.3 assumes the running mean of the fringes to be truth, hence will not be compatible with the existing *JWST* pipeline reference files.

Figure 4 demonstrates the issues discussed. We show four different spectra in 11 of the 12 MRS spectral bands (1A to 4B, excluding 4C due to low SNR):

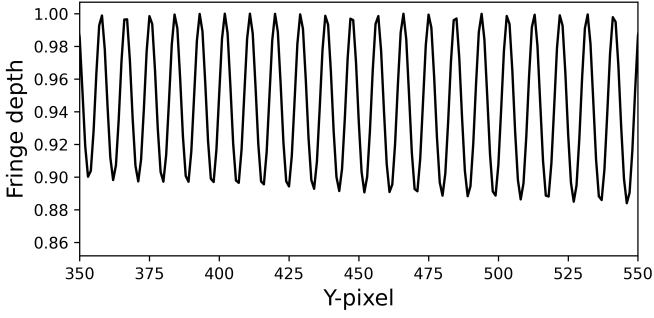


Fig. 3. Depth of the commissioning fringe flat in band 1A. The values on the y-axis are the correction factors by which the data is divided in the pipeline.

- "Photon conversion efficiency": The MIRI FM ground testing derived photon conversion efficiency values normalised per band. At $8\ \mu\text{m}$ an artefact from the MIRI MTS is visible.
- "No PHOTOM": These spectra shows the extracted spectrum of the G dwarf HD 159222 after reducing the data with a PSFF and without applying the photom step in the *JWST* pipeline. The shape and most of the features correspond to those of the ground spectral response, excluding the $8\ \mu\text{m}$ artefact which is no longer present in the data.
- "Commissioning PHOTOM": Extracted spectra when applying the PSFF, as well as the commissioning version of the PHOTOM reference files. Fringes in band 2C are introduced by the photom step; in this case the fringes are present in the PHOTOM calibration reference file. Also importantly, the change in the choice of fringe flat (pipeline versus new PSFF), with different assumptions about the true signal, results in the PHOTOM files not being applicable, which in turns results in the spectra showing a prominent curvature in each spectral band.
- "PSFF PHOTOM": Spectra extracted after applying the PSFF together with the re-derived PHOTOM reference files based on HD 163466.

Below, we describe how we re-derived the PHOTOM reference files based on HD 163466, after self-calibrating by applying the new fringe flat files derived from HD 163466 itself. Due to the 2-dimensional response of the detector, which is incorporated into the spatially extended background signal, the annulus background subtraction will not be accurate here. The aim is therefore to remove the influence of the 2-dimensional response in the background, on the detector image plane prior to the spectrophotometric calibration, by using the dedicated background observations. To minimise the contribution of noise from the dedicated background observations linked to HD 163466, a smooth 2-dimensional polynomial is fitted per dispersed slice of signal on the detector. Since the background has already been subtracted in this case, the spectra are extracted without an annulus. Since no annulus is used, a modified set of aperture correction factors is included into the calculations to account for this.

For most parts of the wavelength range, the use of the dedicated backgrounds works well. However, the spatial and spectral structure of the stronger thermal background in channel 4 does not match between the dedicated background and the target observation. Due to the large resulting (structured) residuals, a different technique is required to subtract the background. Here, the large drop in quantum efficiency in channel 4 is exploited; by subtracting individual dithers from each other, the background

can be decoupled and removed from the signal on the source (the used technique is similar to chop-nodding for ground based infrared telescopes). We illustrate the procedure in Fig. 5. Since the signal is not as strong in channel 4 for the A star, the PSF wings are not detected and the resulting negative PSFs do not significantly overlap with the signal. We note that this cannot be done for targets that are bright at the longer wavelengths, as the overlap of the PSF wings becomes more significant here. However, to fully mitigate the effect of the negative PSFs, the spectra in channel 4 are extracted with a $1.25\times\lambda/D$ aperture, instead of $2.5\times\lambda/D$. Additionally, it should be noted that due to the low signal in channel 4, the resulting spectra are noisy and the reference files not as robust as for the other channels. Furthermore, this method is only applied for the PSFF case, all other spectra are extracted using the standard aperture-annulus method described in Sect. 2.4.

By defining a spline through hand-selected points on the continuum of HD 163466, the spline-fitted continuum is divided by a model spectrum of the continuum of HD 163466 Bohlin et al. (2017, 2020). The accuracy of PHOTOM is therefore limited by the precision of the assumed model. The resulting wavelength-dependent factors are used as the new PHOTOM correction applied on the G dwarf. This process is illustrated in Fig. 6. We can safely assume that the systematics in the continuum of the PHOTOM-uncalibrated spectrum are due to the MRS optical chain transmission and the detector response, as presented in Fig. 4. The two match quite well, aside from the water feature at $8\ \mu\text{m}$ (artefact from the FM ground test campaign).

A spectral leak is present in the data of HD 163466, and in fact in all MRS data. In the case of HD 163466, this impacts the PHOTOM solution, hence it is even more important to address it. The transmission profile of the MRS dichroics causes a spectral leakage of the $m=2$ grating order being superimposed on the $m=1$ grating order. Quantitatively, 2.5% of the spectral flux density at $6.1\ \mu\text{m}$ (see system transmission based on lab data of dichroic transmission curves Fig. 7) is added to the $12.2\ \mu\text{m}$ wavelengths (band 3A). For further details, we refer the reader to Argyriou (2021), Sect. 7.3. Due to this, also visible in Fig. 4, the increase in flux is folded into the commissioning PHOTOM reference file in band 3A, resulting in an underestimated correction factor around this wavelength. To remove this feature from the newly derived PHOTOM files, we find the fraction of flux from band 1B that is present in 3A using the transmission of the optical path shown in Fig. 7.

Since we know that the flux per band is equal to the signal S times the correction factors P , the fluxes F are

$$\begin{aligned} F_{1B}(\lambda_{1B}) &= S_{1B}(\lambda_{1B}) \cdot P_{1B}(\lambda_{1B}), \\ F_{3A}(\lambda_{3A}) &= S_{3A}(\lambda_{3A}) \cdot P_{3A}(\lambda_{3A}), \end{aligned} \quad (1)$$

and inversely

$$\begin{aligned} P_{1B}(\lambda_{1B}) &= \frac{F_{1B}(\lambda_{1B})}{S_{1B}(\lambda_{1B})}, \\ P_{3A}(\lambda_{3A}) &= \frac{F_{3A}(\lambda_{3A})}{S_{3A}(\lambda_{3A})}. \end{aligned} \quad (2)$$

The flux in the leak L is related to the transmission T_{sys} as

$$L_{1B}(\lambda_{1B}) = F_{1B}(\lambda_{1B}) \cdot T_{\text{sys}}(\lambda_{1B}) = S_{1B}(\lambda_{1B}) \cdot P_{1B}(\lambda_{1B}) \cdot T_{\text{sys}}(\lambda_{1B}). \quad (3)$$

Since the spectral leak in the A star results in a positive bump in the spectrum, the PHOTOM factors are underestimated by a

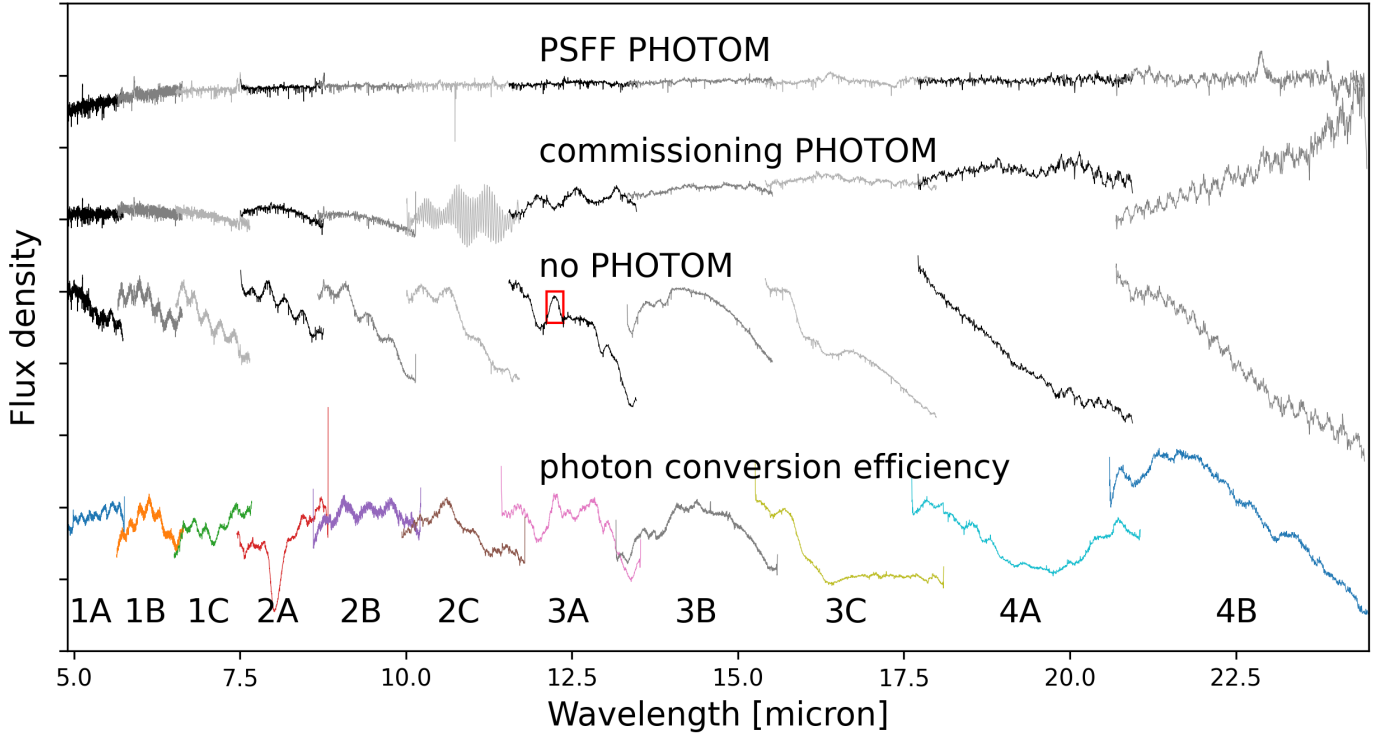


Fig. 4. Comparison between the different ways of reducing the data of HD 159222 with the dedicated fringe flat. From bottom to top: the photon conversion efficiency of the MIRI MRS detectors; the reduction without spectrophotometric calibration (PHOTOM) applied; the results after applying the commissioning PHOTOM; and the new dedicated PHOTOM. Band 4C is omitted due to low signal. The red box indicates the spectral leak.

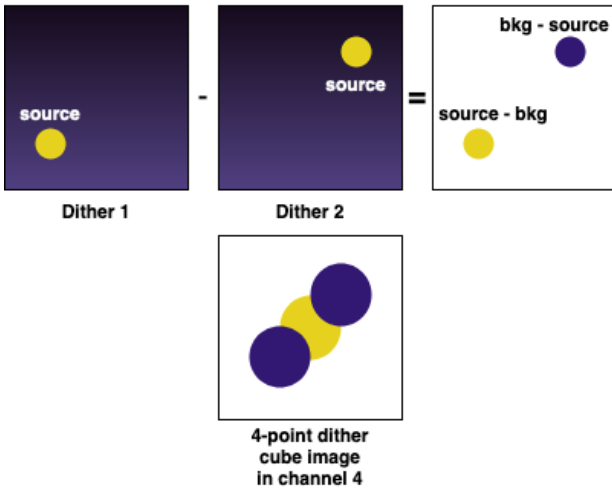


Fig. 5. Illustration of the 4-point dither subtraction to remove the background. Two pairs of the largest separated dithers (dither 1 – 2, dither 2 – 1; and dither 3 – 4, dither 4 – 3), are subtracted from one another to remove the background. This leaves a clean, positive PSF, and a negative one. Due to the size of the PSF in channel 4 the negative and positive signal overlap, therefore a smaller aperture is used to extract the spectrum.

factor

$$P_{3A,corr} = \frac{[L_{1B}(\lambda_{1B})](\lambda_{3A})}{S_{3A}(\lambda_{3A})} = \frac{[S_{1B}(\lambda_{1B}) \cdot P_{1B}(\lambda_{1B}) \cdot T_{sys}(\lambda_{1B})](\lambda_{3A})}{S_{3A}(\lambda_{3A})}, \quad (4)$$

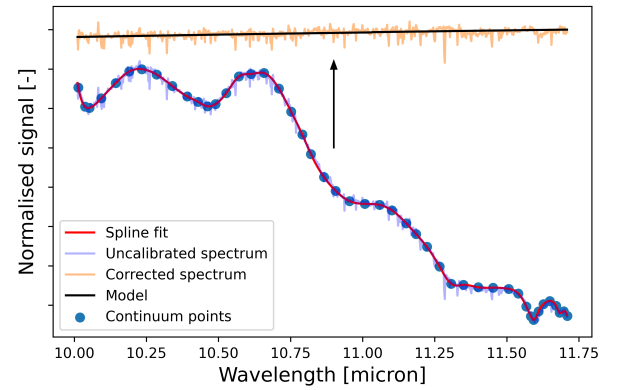


Fig. 6. Illustration of the process of the derivation of the new PHOTOM. This example shows band 2C. The spectrum was normalised with respect to its maximum, and is unit-less. A spline is fitted through the chosen continuum points on the spectrum. This spline is then divided by the model spectrum, to find the correction factors. The result from multiplying the uncalibrated spectrum by these factors (indicated by the arrow) is shown in orange, and matches the model.

which are added to the PHOTOM factors found from fitting the spline to the continuum:

$$P_{3A,new} = P_{3A,old} + P_{3A,corr}. \quad (5)$$

Aside from removing the spectral leak artefact from the reference files, the leak from the target itself must also be removed from the spectrum. Following the relations mentioned above, the extra flux is removed using:

$$F_{3A,new}(\lambda_{3A}) = F_{3A,old}(\lambda_{3A}) - [L_{1B}(\lambda_{1B})](\lambda_{3A}). \quad (6)$$

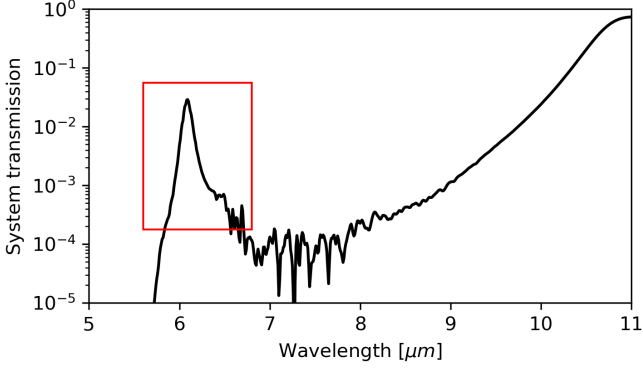


Fig. 7. Transmission of the MRS optical path to sub-band 3A. A leak is seen around $6.1 \mu\text{m}$, indicated by the red box.

Note that in both cases, the location of the leak in the had to be shifted by $0.03 \mu\text{m}$ to match the location of the "bump" in the spectrum. The new spectrum is shown at the top of Fig. 4.

2.6. Synthetic spectra

The synthetic spectra showing the transitions of CO, SiO and OH in Figs. 9, 10, 11 and 12 are based on hydrostatic models taken from the COMARCS grid for cool stars (Aringer et al. 2016). In the case of HD 37122 we used a computation with $T_{\text{eff}} = 4000 \text{ K}$ and $\log(g [\text{cm/s}^2]) = 1.54$. For HD 159222 the corresponding values are $T_{\text{eff}} = 5800 \text{ K}$ and $\log(g [\text{cm/s}^2]) = 4.40$. Both models have solar abundances and one solar mass. The microturbulent velocity was set to 2.5 km/s . We want to note that these properties were chosen to obtain spectra similar to those of the two selected stars. No fit of the MRS or any other observed data has been made. The molecular spectra were calculated from the original model structures by including only the line opacities of the corresponding species in the radiative transfer. For CO the data are taken from Li et al. (2015), for SiO from ExoMol (Barton et al. 2013), and for OH from HITEMP (Rothman et al. 2010). The original resolution of $R = 200000$ was reduced by a convolution to match the MRS observations.

3. Results

3.1. Propagated noise from the empirical fringe flat

Since no filtering was performed to create the PSFF, remaining noise is propagated to the G dwarf spectrum when applying the correction. In order to examine the extent of this effect, we find the standard deviation of the noise around the continuum. The smaller the standard deviation, the less noisy the spectrum is. Due to a known issue with the MRS pointing repeatability (Argyriou et al., in prep., and references therein), there is an offset between the observations of the G and A stars in channel 1 on the detector. Because of this offset, the PSF is sampled differently which results in a change in the resulting fringe pattern (see Sect. 2.3), the correction is not expected to work as well. While a pointing offset would compromise the fringe correction in all channels, the requirement is especially stringent in channel 1 due to undersampling of the PSF. Additionally, the PHOENIX model (Bohlin et al. 2017, 2020) shows a dense forest of features in this wavelength range, making it difficult to distinguish noise from real features. We will therefore examine the noise in channel 2 and onward.

Table 2. Standard deviation of the noise after removing the continuum. The values, from left to right, correspond to the two pipeline approaches: the fringe flat including the residual fringe correction; and the PSFF.

Band	σ (ff+rfc / PSFF)
2A	0.0082 / 0.0086
2B	0.0068 / 0.0071
2C	0.0076 / 0.0076
3A	0.0075 / 0.0064
3B	0.0066 / 0.0057
3C	0.0070 / 0.0069

The properties of the noise, presented in Table 2, show the most significant change between applying the fringe flat and residual fringe correction and the method presented in this work. Residual fringes in the spectrum result in a larger spread around the mean. The PSFF spectrum does not seem to contain more noise, despite the noise in the correction. In terms of noise the performance of the PSFF is comparable to that of the pipeline fringe flat (based on a spatially homogeneous and extended source) with a residual fringe correction.

3.2. Performance of fringe removal

When the fringes are removed by the fringe flat and residual fringe correction, no components linked to the detector geometric and refractive properties should remain, and no new frequencies should be added. From the estimated residual fringe contrast we can find how the different reduction methods compare. The results of this process are presented in Fig. 8.

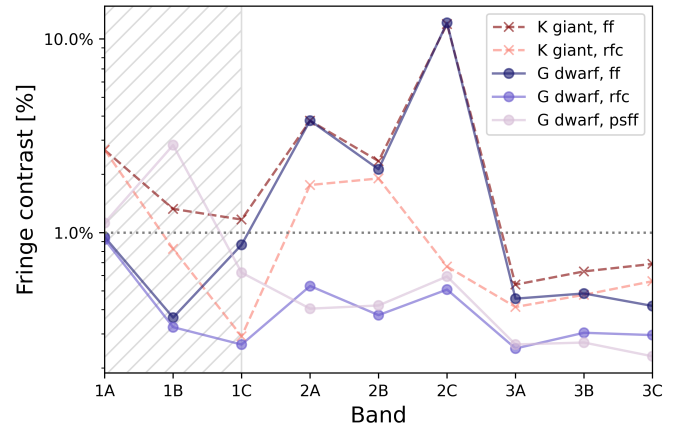


Fig. 8. Fringe contrast after the different corrections presented in this work. "ff" stands for fringe flat, "rfc" for fringe flat and the residual fringe correction applied, and finally "ps" denotes the PSFF. The contrasts in channel 1 are shaded, since the pointing repeatability issue results in larger residuals in the PSFF case.

We already noted the pointing issues in channel 1, and this is confirmed by the larger fringe residual after applying the PSFF. When looking at the longer wavelength bands, where we do expect a relatively good correction, it is evident that the performance is similar to the fringe flat plus residual fringe correction, reaching sub-percent level residuals for the G dwarf. Therefore, the PSFF method results in comparable residuals.

On the other hand, the K giant clearly shows larger contrasts even after applying the residual fringe correction, particularly in bands 1A, and 2A/B. This shows that these results are target-

specific. The K giant is dense in features, as will be demonstrated in Sect. 3.3, and the residual fringe correction may either not affect certain sections, or potentially remove or reduce the strength of molecular bands. This can be a risk if the periodicities of the molecular bands and the fringes overlap. We take a closer look at this issue by discussing the periodograms of the stellar and synthetic spectra.

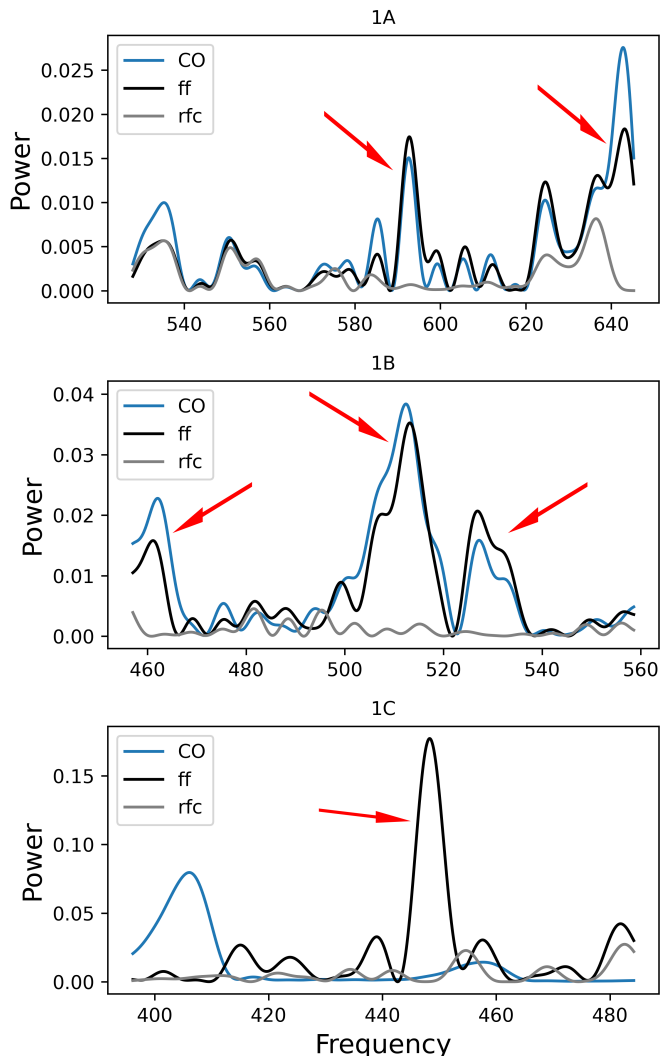


Fig. 9. Periodograms of the synthetic CO spectrum and the K giant spectrum per MRS band, before and after residual fringe correction. "ff" stands for fringe flat, and "rfc" for fringe flat and the residual fringe correction. The frequency range shown is the range where the `residual_fringe` pipeline algorithm searches for frequencies to remove. The red arrows indicate the largest peaks that are removed by the algorithm.

In Fig. 9, we present the periodograms generated using `LombScargle` of `astropy` (Astropy Collaboration et al. 2013, 2018). The periodograms of the K giant spectrum after applying only the pipeline fringe flat and after applying the additional residual fringe correction, are shown alongside the periodogram of the CO synthetic spectrum. Comparing the profiles, it can be concluded that the CO signal in the spectrum has been directly affected by the residual fringe correction in the cases of band 1A and 1B, but not in 1C. The largest peaks removed by the algorithm are indicated by the red arrows. These overlap with strong peaks in the periodogram of CO in bands 1A and 1B. These

peaks are present in the spectrum with only the fringe flat applied, and removed after applying the residual fringe correction. In 1C, a detector fringe seems to be removed instead. Therefore, aside from performing similarly in terms of fringe residuals, using the PSFF mitigates the risk of removing molecular features.

This exercise can be done for all examined MRS bands where the molecular species show prominent features, and rather than showing the periodograms separately, we take the difference between before and after applying the residual fringe correction, to demonstrate where the largest differences occur. If this change overlaps with a peak in the molecular periodogram, it is likely that real features are affected rather than solely the detector fringes. The results are included in Fig. A.1 of App. A.

3.3. Detectability of molecular features

The resulting normalised spectra for both the G dwarf and the K giant are presented in Fig. 10. The top panel of Fig. 10 shows the K giant, the bottom panel the G dwarf. Fig. 11 and Fig. 12 include closer comparisons for the K giant of the continuum-divided stellar spectra and the synthetic spectra of CO, SiO, and OH.

While previously more detailed statistics regarding the corrections were discussed, these spectra in Fig. 10 demonstrate the global effects of the different methods on the spectra directly. In band 2C the commissioning PHOTOM files introduced fringes, which are subsequently removed by the residual fringe correction. The aim is to fix this issue during Cycle 1.

Previously, the risk of the residual fringe correction removing or altering features was mentioned. However, the positive impact is also visible. For the K giant, this is best demonstrated in the third panel of Fig. 11, where the large fringes initially masked OH features. At the shorter wavelengths, particularly in the spectrum of the K giant, the signal is seemingly noisy. This is due to the presence of CO, as shown in Fig. 11. In addition to the CO bands, the SiO dip around $8\ \mu\text{m}$ is clearly visible in Fig. 10. While the *Spitzer* IRS spectrum already shows the drop in flux around $5\text{--}6\ \mu\text{m}$ due to CO, the dip from SiO around $8\text{--}10\ \mu\text{m}$, and the OH features longward of $14\ \mu\text{m}$; the detailed views of the MRS spectrum in Fig. 11 demonstrate how well we are now able to observe the structure in the spectrum of the K giant, as it matches the synthetic spectra very well.

On the other hand, the G dwarf is less rich in features, due to its higher effective temperature, evident in the flat CO spectrum in Fig. 12. The features of SiO and OH are not detected in this temperature range (see Fig. 10). While similar improvements are observed between the fringe flat and addition of the residual fringe correction, in the top-most spectrum of the bottom panel of Fig. 10, only the PSFF was applied to the data. The previous sections discussed how statistically the correction performs well, but here the visual effect on the spectrum is shown. It is evident that, with just one correction, a clean spectrum is achieved. However, the caveat related to the pointing offset in channel 1 is also visible as residual fringing.

In order to better quantify improvements in the data reduction and strength of the features in the spectra, we perform cross-correlations with the synthetic spectra discussed in Sect. 2.6 and find the resulting SNR of the detection. First, the spectra are binned to the same resolution as the observations, using `SpectRes` (Carnall 2017). The continuum of both the synthetic spectra and the observations is removed using a running mean, such that only the structure of the molecular bands is correlated. The cross-correlation is done with the standard `numpy.correlate` function. By dividing the maximum corre-

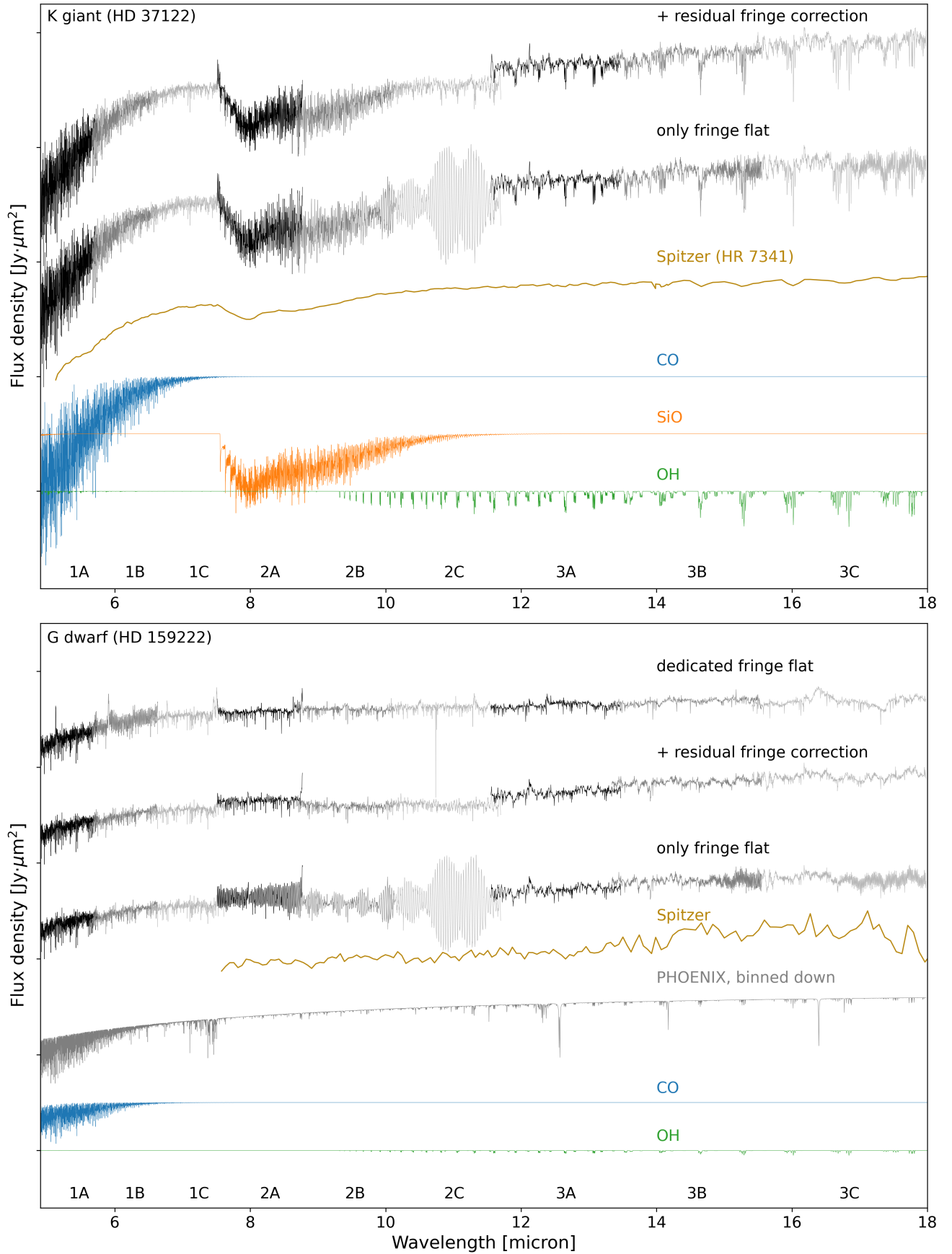


Fig. 10. Spectra for HD 37122 (top) and HD 159222 (bottom), after applying only the extended fringe flat, fringe flat and residual fringe correction, or the point source specific correction labelled "dedicated fringe flat"). The y-axis is in Rayleigh-Jeans units, resulting in a flat tail of the stellar spectrum. The sub-bands (A, B, C) are indicated by increasingly light colours; blue, orange, and green are the model CO, SiO, and OH spectra, respectively. The *Spitzer* spectra are taken from Sloan et al. (2015) (top panel) and the *CASSIS* database (Lebouteiller et al. 2011) (bottom panel).

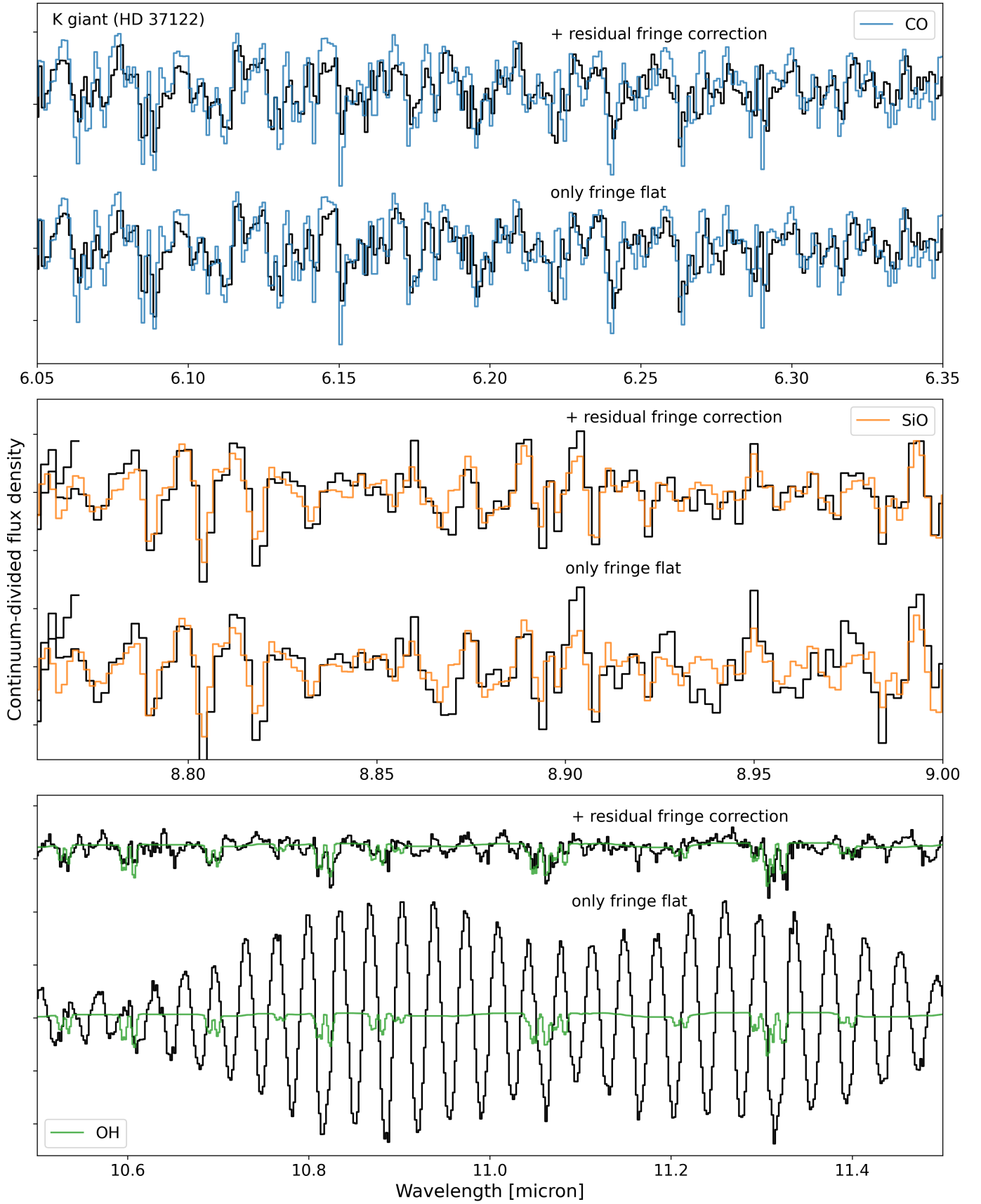


Fig. 11. Close-ups of the spectra of HD 37122, with the continuum removed. The bottom spectrum in each plot includes only the extended fringe flat, and the top both the fringe flat and residual fringe correction. CO, SiO, and OH have been over-plotted.

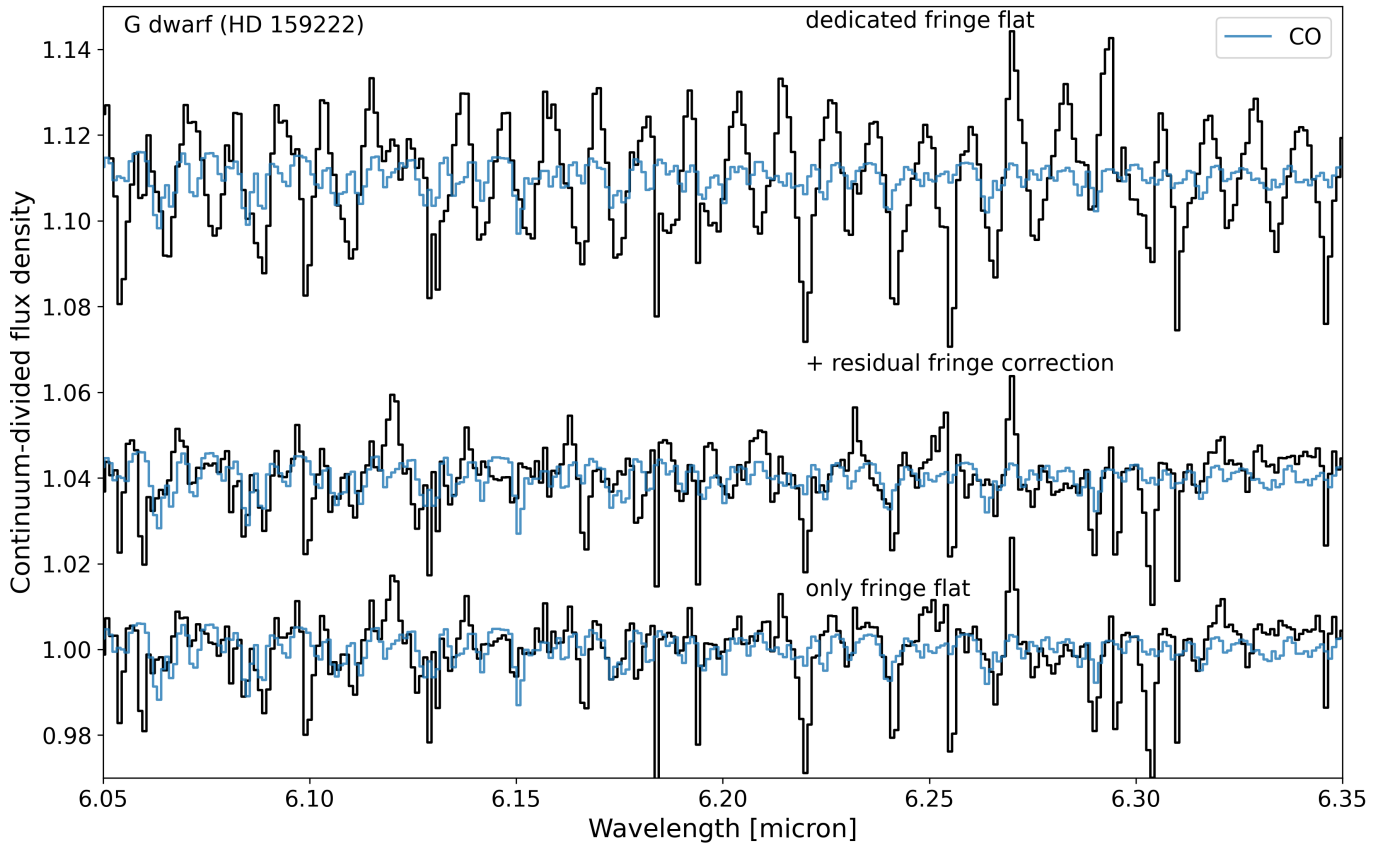


Fig. 12. Close-ups of the spectra of HD 159222, with the continuum removed. The bottom spectrum includes only the extended fringe flat, the middle both the fringe flat and residual fringe correction, and the top the top the point source fringe flat. CO has been over-plotted.

lation factor by the standard deviation of the noise, we find the SNR of the feature, similarly to Petrus et al. (2021) and Patapis et al. (2022). However, we note that since the fringes in the spectrum are not random in nature, the Gaussian approximation of the noise may not be entirely accurate in cases where large fringe residuals remain.

The SNR values are summarised in Table 3. In some bands the pipeline fringe flats leave large residuals, and the cross-correlations are not able to find the molecular signal in the spectrum. For example, in the extreme case of band 2C of the K giant HD 37122 the SNR of the OH detection drastically increases after running the residual fringe step. However, the results of both reductions are similar, showing that generally the presence of some residual fringes does not prevent the detection of these relatively strong features. In fact, in the K giant all three of the molecules are detected, with SNRs near 10 or higher.

Interestingly, in some cases the SNR is reduced after applying the residual fringe correction. This is most significant in the CO detections in bands 1A and 1B, and OH in 3A. In Sect. 3.2 it was demonstrated that some part of the periodogram of CO overlapped with the expected fringe frequencies. In fact, peaks in the same location as those of CO were removed by the residual fringe correction in 1A and 1B while remaining untouched in 1C, indicating that the nature of the CO features was altered by the algorithm in these cases. It is therefore possible that the reduced SNR is due to this change. These results also show why the SNR is increased in other cases, in bands 1C, and 2A–C in Fig. A.1 the largest difference between the two corrections occurs in locations where no strong molecular peaks are found. While the effect in the demonstrated cases is relatively small—

detection was not prevented by the residual fringe correction—the impact and limitations of the algorithm must be considered when examining spectra.

In the G dwarf a significant SNR is found for CO only in bands 1A and 1B. Due to the higher stellar effective temperature, the CO features are weaker, and quickly disappear into the noise. Due to the performance of the PSFF in channel 1, a decrease in SNR is observed compared to the other two reduction methods. Additionally, the same issue is seen here as in the K giant, where the SNR decreases between fringe flat and residual fringe correction. This is also visible in the match between the synthetic spectrum and the different spectra in Fig. 12 (for example before $6.15 \mu\text{m}$, where a bump is removed from the spectrum between the fringe flat and residual fringe correction).

4. Discussion

We found the PSFF to work most effectively in channels 2 and 3, and less well in channel 1 due to the MRS pointing non-repeatability, with relatively high remaining fringe contrast especially in band 1B and 1C (see Fig. 8). Channel 1 has the most stringent requirement on accuracy of target acquisition for the PSFF due to the MRS PSF being spatially under-sampled by design. It remains to be seen to what extent we will be able to improve our ability to use empirical PSFFs in channel 1, where the pointing offset resulted in percent-level residuals, rather than sub-percent (see Fig. 8). Currently, there is not enough data to constrain how large the pointing offset may be for the method to work correctly. Regardless, it is required to use target acquisition to apply this method. Especially when considering features

Table 3. SNRs of the cross-correlations between the synthetic molecular spectra and the different spectral bands. The first number corresponds to the data without the residual fringe correction, while the second includes the extra residual fringe correction step. The third value in the G dwarf rows denotes the cross-correlation from the point source fringe flat. Entries marked with a dash indicate that there are no significant features in this band, or no significant SNR was found.

K giant (HD 37122)									
	1A	1B	1C	2A	2B	2C	3A	3B	3C
CO	19.6 / 19.1	15.7 / 13.6	6.9 / 7.8	-	-	-	-	-	-
SiO	-	-	-	8.8 / 9.4	10.9 / 11.3	3.7 / 5.2	-	-	-
OH	-	-	-	-	-	3.7 / 10.9	8.5 / 7.9	10.9 / 10.1	11.5 / 11.5
G dwarf (HD 159222)									
CO	14.2 / 13.7 / 13.4	9.0 / 7.5 / 4.0	-	-	-	-	-	-	-
OH	-	-	-	-	-	-	-	-	-

potentially being removed by the residual fringe correction, or altered as was shown here, the PSFF may still be the preferred method for fringe removal in the future in channel 2, 3, and 4.

Aside from the risk of the period of the real spectral features overlapping with those of the detector fringes, filtering out a sinusoid can still indirectly change other parts of the spectrum. This, and the aforementioned problem where the residual fringe algorithm directly changes parts of a molecular feature, is likely not stringent for most applications, but can become important when searching for fainter features. Additionally, feature-rich spectra may not be corrected well by the residual fringe correction, in which case the PSFF is the preferred method.

Care must be taken when deriving a PSFF. We already touched upon the difficulties and consequences of this process in Sect. 2.5. For a perfect correction any spectral lines must be removed, and the reference data must be filtered to reduce noise, which would otherwise be propagated into the spectrum. Although in Sect. 3.1 we did not find any significant increases in the noise levels, it is still advised to find a way to remove the noise. We did not do this here, but we aim to improve our methods for future work.

Finally, the commissioning PHOTOM files have some issues, like re-introducing fringes in band 2C (see Sect. 2.5). In future versions these issues can be ironed out, by deriving the reference files from scratch in-flight. By doing so, features introduced in the PHOTOM files long ago will no longer be present. We already presented a method here to do this specifically for point sources in a particular dither pattern, but we must fully probe the 2D response of the detector to be able to apply the new PHOTOM files to all other targets. Ideally, this would be done with fully extended, uniform illumination of the detectors, where the flux is known. However, no such target exists in space, and our best calibrators are hot stars with continuum close to a blackbody. Therefore, to characterise the 2D response of the detectors, a large data set is required where the star is raster scanned on many locations on the detector. Finally, one downside of using stellar spectra, is their relatively low flux farther in the mid-infrared. The lack of signal in channel 4 results in a noisy reference spectrum, or zero flux in these ranges, making the process of calibrating them more difficult. The use of asteroids, i.e. bright red spectra with very broad spectral features, could potentially improve the fringe calibration and MRS ASRF at the longest wavelengths.

5. Conclusions

In this paper we presented some of the first stellar MIRI MRS spectra taken during the commissioning phase of *JWST*. We have also shown the importance of a suitable fringe correction

for unresolved sources. The pipeline approach (fringe flat + residual fringe correction) does remove most of the fringe signal and allows the detection of molecular species. While the method is suitable for most applications, there is a risk of periodic features similar to the expected fringe pattern being weakened or removed by the residual fringe algorithm. Especially for point sources, a suitable empirical fringe flat has the potential to out-perform the pipeline approach and provide a higher fidelity correction when required, limited by the reproducibility of the pointing. This approach does not rely on fitting and removing periodic features, making it an inherently safer approach when analysing spectra with highly periodic features.

Intricately linked to the fringes is the spectrophotometric calibration. We demonstrated that a clean on-sky calibration is possible for point sources. This method will be extrapolated to a larger data set to probe and characterise the 2D response of the detectors, to create clean files applicable to spatially extended targets observed with the MRS.

Finally, we examined the impact of different fringe correction methods on the detectability of CO, SiO, and OH in the spectra of the K giant HD 37122; and CO in the G dwarf HD 159222. The molecular bands are resolved, after effectively removing the fringes. However, we did note a change in the molecular features due to parts of the frequency spectrum being removed by the residual fringe correction. Though this change is subtle and will not impact most science cases, it is something to look out for when running the algorithm.

Acknowledgements. The authors thank Prof. dr. Ewine van Dishoeck for useful comments and suggestions that helped improve the quality of the work presented. Danny Gasman, Ioannis Argyriou, Bart Vandenbussche, and Pierre Royer, thank the European Space Agency (ESA) and the Belgian Federal Science Policy Office (BELSPO) for their support in the framework of the PRODEX Programme. J.A.-M. and A.L. acknowledge support by grant PIB2021-127718NB-I00 from the Spanish Ministry of Science and Innovation/State Agency of Research MCIN/AEI/10.13039/501100011033 and by “ERDF A way of making Europe”. P.J.K. acknowledges financial support from the Science Foundation Ireland/Irish Research Council Pathway programme under Grant Number 21/PATH-S/9360. The work presented is the effort of the entire MIRI team and the enthusiasm within the MIRI partnership is a significant factor in its success. MIRI draws on the scientific and technical expertise of the following organisations: Ames Research Center, USA; Airbus Defence and Space, UK; CEA-Irfu, Saclay, France; Centre Spatial de Liège, Belgium; Consejo Superior de Investigaciones Científicas, Spain; Carl Zeiss Optronics, Germany; Chalmers University of Technology, Sweden; Danish Space Research Institute, Denmark; Dublin Institute for Advanced Studies, Ireland; European Space Agency, Netherlands; ETCA, Belgium; ETH Zurich, Switzerland; Goddard Space Flight Center, USA; Institut d’Astrophysique Spatiale, France; Instituto Nacional de Técnica Aeroespacial, Spain; Institute for Astronomy, Edinburgh, UK; Jet Propulsion Laboratory, USA; Laboratoire d’Astrophysique de Marseille (LAM), France; Leiden University, Netherlands; Lockheed Advanced Technology Center (USA); NOVA Opt-IR group at Dwingeloo, Netherlands; Northrop Grumman, USA; Max-Planck Institut für Astronomie (MPIA), Heidelberg, Germany; Laboratoire d’Etudes Spatiales et d’Instrumentation en Astrophysique (LESIA), France; Paul Scher-

rer Institut, Switzerland; Raytheon Vision Systems, USA; RUAG Aerospace, Switzerland; Rutherford Appleton Laboratory (RAL Space), UK; Space Telescope Science Institute, USA; Toegest- Natuurwetenschappelijk Onderzoek (TNO-TPD), Netherlands; UK Astronomy Technology Centre, UK; University College London, UK; University of Amsterdam, Netherlands; University of Arizona, USA; University of Bern, Switzerland; University of Cardiff, UK; University of Cologne, Germany; University of Ghent; University of Groningen, Netherlands; University of Leicester, UK; University of Leuven, Belgium; University of Stockholm, Sweden; Utah State University, USA. A portion of this work was carried out at the Jet Propulsion Laboratory, California Institute of Technology, under a contract with the National Aeronautics and Space Administration.

We would like to thank the following National and International Funding Agencies for their support of the MIRI development: NASA; ESA; Belgian Science Policy Office; Centre Nationale D'Etudes Spatiales (CNES); Danish National Space Centre; Deutsches Zentrum für Luft-und Raumfahrt (DLR); Enterprise Ireland; Ministerio De Economía y Competitividad; Netherlands Research School for Astronomy (NOVA); Netherlands Organisation for Scientific Research (NWO); Science and Technology Facilities Council; Swiss Space Office; Swedish National Space Board; UK Space Agency.

We take this opportunity to thank the ESA *JWST* Project team and the NASA Goddard ISIM team for their capable technical support in the development of MIRI, its delivery and successful integration.

This work has made use of data from the European Space Agency (ESA) mission *Gaia* (<https://www.cosmos.esa.int/gaia>), processed by the *Gaia* Data Processing and Analysis Consortium (DPAC, <https://www.cosmos.esa.int/web/gaia/dpac/consortium>). Funding for the DPAC has been provided by national institutions, in particular the institutions participating in the *Gaia* Multilateral Agreement.

This work is based on observations made with the NASA/ESA/CSA James Webb Space Telescope. The data were obtained from the Mikulski Archive for Space Telescopes at the Space Telescope Science Institute, which is operated by the Association of Universities for Research in Astronomy, Inc., under NASA contract NAS 5-03127 for *JWST*; and from the European *JWST* archive (eJWST) operated by the ESAC Science Data Centre (ESDC) of the European Space Agency. These observations are associated with program #1029, 1050.

References

- Álvarez-Márquez, J., Labiano, A., Guillard, P., et al. 2022, Nuclear High-Ionization Outflow in the Compton-Thick AGN NGC 6552 as seen with *JWST* Mid-Infrared Spectroscopy
- Ardila, D. R., Van Dyk, S. D., Makowiecki, W., et al. 2010, *ApJS*, 191, 301
- Argyriou, I. 2021, Calibration of the MIRI instrument on board the James Webb Space Telescope, https://fys.kuleuven.be/ster/pub/phd-thesis-yannis-argyriou/PhD_Thesis_IoannisArgyriou.pdf
- Argyriou, I., Rieke, G. H., Ressler, M. E., Gáspár, A., & Vandenbussche, B. 2020a, in Society of Photo-Optical Instrumentation Engineers (SPIE) Conference Series, Vol. 11454, Society of Photo-Optical Instrumentation Engineers (SPIE) Conference Series, 114541P
- Argyriou, I., Wells, M., Glasse, A., et al. 2020b, *A&A*, 640, A150
- Aringer, B., Girardi, L., Nowotny, W., Marigo, P., & Bressan, A. 2016, *MNRAS*, 457, 3611
- Astropy Collaboration, Price-Whelan, A. M., Sipőcz, B. M., et al. 2018, *AJ*, 156, 123
- Astropy Collaboration, Robitaille, T. P., Tollerud, E. J., et al. 2013, *A&A*, 558, A33
- Barton, E. J., Yurchenko, S. N., & Tennyson, J. 2013, *MNRAS*, 434, 1469
- Bohlin, R. C., Hubeny, I., & Rauch, T. 2020, *AJ*, 160, 21
- Bohlin, R. C., Mészáros, S., Fleming, S. W., et al. 2017, *AJ*, 153, 234
- Carnall, A. C. 2017, arXiv e-prints, arXiv:1705.05165
- Cohen, M., Megeath, S. T., Hammersley, P. L., Martín-Luis, F., & Stauffer, J. 2003, *AJ*, 125, 2645
- Decin, L., Morris, P. W., Appleton, P. N., et al. 2004, *ApJS*, 154, 408
- Decin, L., Vandenbussche, B., Waelkens, C., et al. 2003, *A&A*, 400
- Fabrizius, C., Luri, X., Arenou, F., et al. 2021, *A&A*, 649, A5
- Gaia Collaboration, Brown, A. G. A., Vallenari, A., et al. 2021, *A&A*, 649, A1
- Gaia Collaboration, Prusti, T., de Bruijne, J. H. J., et al. 2016, *A&A*, 595, A1
- García-Bernete, I., Rigopoulou, D., Alonso-Herrero, A., et al. 2022, *A&A*, 666, L5
- Gardner, J. P., Mather, J. C., Clampin, M., et al. 2006, *Space Sci. Rev.*, 123, 485
- Gordon, K. D., Bohlin, R., Sloan, G. C., et al. 2022, *AJ*, 163, 13
- Gray, R. O., Corbally, C. J., Garrison, R. F., McFadden, M. T., & Robinson, P. E. 2003, *AJ*, 126, 2048
- Heras, A. M., Shipman, R. F., Price, S. D., et al. 2002, *A&A*, 394, 539
- Houck, J. R., Roellig, T. L., van Cleve, J., et al. 2004, *ApJS*, 154, 18
- Kester, D. J. M., Beintema, D. A., & Lutz, D. 2003, in The Calibration Legacy of the ISO Mission, ed. L. Metcalfe, A. Salama, S. B. Peschke, & M. F. Kessler, Vol. 481, 375
- Labiano, A., Argyriou, I., Álvarez-Márquez, J., et al. 2021, *A&A*, 656, A57
- Labiano, A., Azzollini, R., Bailey, J., et al. 2016, in Observatory Operations: Strategies, Processes, and Systems VI, Vol. 9910, Proc. The MIRI Medium Resolution Spectrometer Calibration Pipeline
- Lahuis, F. & Boogert, A. 2003, in , ed. C. L. Curry & M. Fich, 335
- Lahuis, F. & van Dishoeck, E. F. 2000, *A&A*, 355, 699
- Lau, R. M., Hankins, M. J., Han, Y., et al. 2022, *Nature Astronomy*, 6, 1308
- Lebouteiller, V., Barry, D. J., Spoon, H. W. W., et al. 2011, *ApJS*, 196, 8
- Li, G., Gordon, I. E., Rothman, L. S., et al. 2015, *ApJS*, 216, 15
- Mahdi, D., Soubiran, C., Blanco-Cuaresma, S., & Chemin, L. 2016, *A&A*, 587, A131
- Malumuth, E., Hill, R., Gull, T., et al. 2003, Publications of the Astronomical Society of the Pacific, 115, 218
- Meixner, M., Gordon, K. D., Indebetouw, R., et al. 2006, *AJ*, 132, 2268
- Miles, B. E., Biller, B. A., Patapis, P., et al. 2022, The JWST Early Release Science Program for Direct Observations of Exoplanetary Systems II: A 1 to 20 Micron Spectrum of the Planetary-Mass Companion VHS 1256-1257 b
- Patapis, P., Nasedkin, E., Cugno, G., et al. 2022, *A&A*, 658, A72
- Petrus, S., Bonnefoy, M., Chauvin, G., et al. 2021, *A&A*, 648, A59
- Porto de Mello, G. F., da Silva, R., da Silva, L., & de Nader, R. V. 2014, *A&A*, 563, A52
- Rigby, J., Perrin, M., McElwain, M., et al. 2022, Characterization of JWST science performance from commissioning
- Rothman, L. S., Gordon, I. E., Barber, R. J., et al. 2010, *J. Quant. Spectr. Rad. Transf.*, 111, 2139
- Sloan, G. C., Herter, T. L., Charmandaris, V., et al. 2015, *AJ*, 149
- Soubiran, C. & Triaud, A. 2004, *A&A*, 418, 1089
- Wells, M., Pel, J. W., Glasse, A., et al. 2015, *PASP*, 127, 646
- Yang, Y.-L., Green, J. D., Pontoppidan, K. M., et al. 2022, CORINOS I: JWST/MIRI Spectroscopy and Imaging of a Class 0 protostar IRAS 15398-3359

Appendix A: Comparison of periodograms

In this appendix, the additional periodograms of the K giant spectra and the molecular synthetic spectra are shown in Fig. A.1. Rather than presenting the periodograms of the spectrum including only the fringe flat and the fringe flat + residual fringe correction separately, the difference between the two is represented by the black line. Each panel shows a different band, and the different coloured lines correspond to the periodograms of the molecules. Since the black line shows the difference between the two corrections, the influence of the residual fringe correction on the periodicity of the spectrum can be seen directly. The top row of the figure is analogous to Fig. 9. When the largest difference, i.e. the strongest peak, overlaps with a strong peak of the molecular periodogram, it is likely that the features were altered in the spectra.

This effect is seen in bands 1A and 1B, as was already mentioned prior in Sect. 8, while this is not the case in 1C. In channel 2 none of the molecular periodograms show strong peaks in the altered frequencies, and are therefore likely not affected. In the longer wavelength channels, here channel 3, the search space is much wider, since a longer period beating on top of the shorter period fringe has to be corrected for. This makes the effect more difficult to see.

Additionally, it is especially evident in channel 3 that not only are frequencies removed, resulting in a positive difference, there are also frequencies added. This demonstrates that filtering out a sinusoid has more complex consequences for the spectrum than just removing a fringe.

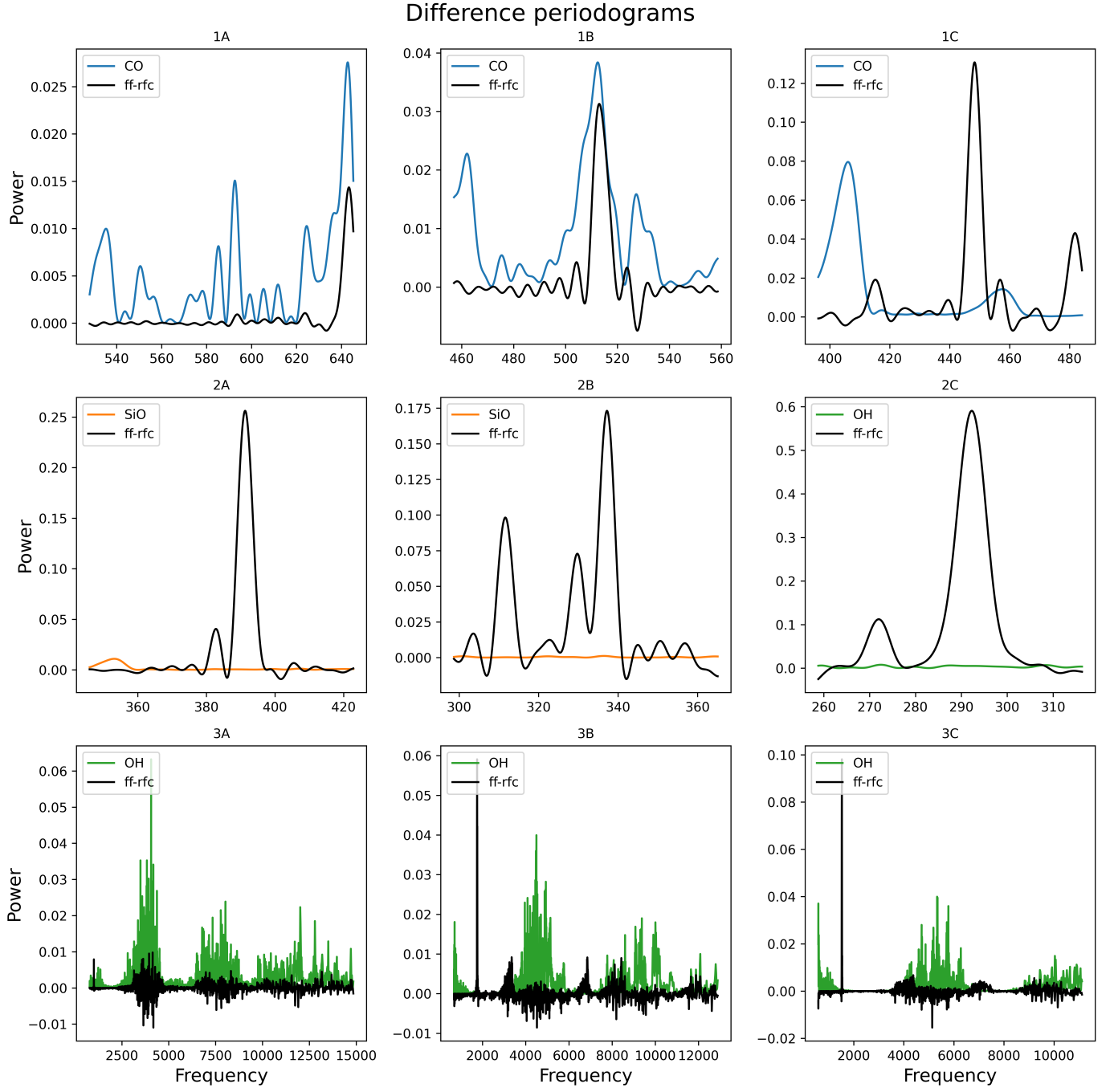


Fig. A.1. Difference between the periodograms of the K giant spectra before and after residual fringe correction per band, compared to the synthetic CO spectrum. "ff" stands for fringe flat, and "rfc" for fringe flat and the residual fringe correction. The section shown is the section where the algorithm searches for strong frequencies to remove.